The unique hybrid precipitate in a peak-aged Al-Cu-Mg-Ag alloy

M.R. Gazizov[1,*], A.O. Boev[2], C.D. Marioara[3], S.J. Andersen[3], R. Holmestad[4], R.O. Kaibyshev[1], D.A. Aksyonov[2], V.S. Krasnikov[5,6]

[1] Belgorod State University, 308015 Belgorod, Russia

[2] Skolkovo Institute of Science and Technology, 143026 Moscow, Russia

[3] Materials and Nanotechnology, SINTEF Industry, N-7465 Trondheim, Norway

[4] Department of Physics, Norwegian University of Science and Technology (NTNU), N-7491 Trondheim, Norway

[5] Chelyabinsk State University, 454001 Chelyabinsk, Russia

[6] South Ural State University (National Research University), 454080 Chelyabinsk, Russia

* Corresponding author: gazizov@bsu.edu.ru

Abstract. The prevalent hardening phase forming in an Al-Cu-Mg-Ag alloy after peak-aging at 150 and 190 °C has been investigated using transmission electron microscopy methods. The precipitate atomic structure was determined. It is a hybrid precipitate (HP) with plate morphology on $\{111\}_{Al}$ planes, consisting of orthorhombic and hexagonal structural fragments. Density functional theory calculations suggest that the hybridization reduces structural incompatibility of the HP plates with the Al matrix at the broad interfacial boundaries. Incorporation of Cu, Mg and Ag in the precipitate lattice provides a reduced formation enthalpy for the HPs.

Keywords: aging; scanning/transmission electron microscopy (STEM); aluminum alloys; precipitation; density functional theory (DFT).

Al-Cu-Mg-Ag alloys are heat-treatable. They exhibit good creep resistance and fracture toughness due to the formation of strengthening precipitates having high resistance to coarsening at elevated temperatures [1–3]. Addition of Mg and Ag to Al-Cu alloys leads to a uniform distribution of disperse, plate-like precipitates called 'Ω', with habit plane $\{111\}_{Al}$.

For the Ω-phase, several nucleation mechanisms have been proposed [4–6]. These include a precursor phase, such as Ω' [4,5], as well as stacking faults arising as a consequence of the Mg and Ag additions [6]. A recent atom probe tomography study [7] has indicated that Ag and Mg co-clusters act as heterogeneous nucleation sites for the Ω phase: During the initial stage of aging, if such co-clusters also contain Cu, Guinier-Preston (GP) zones will form on $\{111\}_{Al}$ planes. A following migration of Ag and Mg to the main plate interfaces correlates with the formation of well-defined Ω plate. A review of literature was unable to find evidence for alternative intermediate phases responsible for nucleating the Ω-phase in Al-Cu-Mg-Ag alloys.

Investigation of the plate-like precipitate formation is interesting since the transformation strains during nucleation of Ω phase can be associated both with a significant shear component (predicted by Aaronson et al. [8] and Nie et al. [9]), as well as with unrelaxed misfit strains normal to the main plate interfaces [3]. Thus, strain accommodation mechanisms play an important role in controlling both nucleation and growth of these plate-like precipitates. To clarify this, improved understanding of the Ω structure and coherency with Al is required. In this work, we show that a unique hybrid precipitate (HP) is important for the alloy strength. We find that the corresponding atomic structure can be described in terms of two structural fragments. This is supported by calculations.

An aluminum alloy with the chemical composition Al-4.5Cu-0.56Mg-0.77Ag-0.42Mn-0.12Ti-0.05V-0.02Fe (wt. %) was prepared using a direct-chill, semi-continuous casting process [10]. The samples were given a solution heat treatment at 510 °C for 1 hour, followed by quenching in water. The samples were aged at 150 °C or 190 °C for different times.

Foils for transmission electron microscopy (TEM) were prepared using conventional methods [11] and studied in two microscopes operated at 200 kV; a JEOL JEM-2100F and a JEOL ARM-200F, the latter being double aberration corrected. The TEM settings given in Table S1 were used for acquisition of STEM images [12].

To refine atom positions and calculate total formation energies for the models suggested, density functional theory (DFT) calculations [13] were performed at 0 K within the projected augmented wave (PAW) formalism [14], generalized gradient approximation of Perdew-Burke-Ernzerhof functional [15] using the Vienna ab initio simulation package (VASP) [16] and SIMAN package [17]. The key parameters are given in Table S2. Relaxation of the atom positions (*p*) but also full (*f*) relaxations (of atom position, cell geometry and volume) were carried out to refine the models. The *p* and *f* relaxations represent two idealized cases: the precipitate/matrix interaction with 'stiff' and 'weak' matrices, respectively. The calculations help estimate the hypothetical interval for the precipitate formation energies. The Al lattice volume was used as a reference.

The initial model was based on an orthorhombic unit cell and morphology. The *z* axis was selected as normal to the $\{111\}_{Al}$ habit plane. The thickness spans 15 $\{111\}_{Al}$ planes. This prevents fault formation in the ABC stacking of the Al matrix, since VASP depends on a periodic repetition of the calculation cell. The approach treats the plates as thin and infinite 2D structures growing on $\{111\}_{Al}$, periodically separated by eight $\{111\}_{Al}$ planes. The formation enthalpy is given as $E_f = E_T - \sum \mu_x n_x$. Here E_T is the total energy of the HP model. μ_X is the chemical potential (cf. Table S3), i.e. the energy when considered as the only solute atom in a similar Al volume. n_x represents the number of atoms of element '*x*' (Al, Cu, Mg or Ag) in the model calculation cell, respectively. Frozen phonon multi-slice simulations were carried out using the MULTEM software and the non-relativistic scattering potentials modified by *Lobato et. al.* [18–20].

In accordance with the hardness curves given for the aging at 150 °C and 190 °C [10] the peak-aging times 1.5 h and 24 h were selected for the TEM analysis, respectively. Close examination of the TEM images revealed two types of plate-like precipitates, which could be categorized by habit planes $\{111\}_{Al}$ and $\{001\}_{Al}$. Fig. 1 gives an example of the $\{111\}_{Al}$ plates seen in a $<211>_{Al}$ zone axis. The minor fraction of the $\{100\}_{Al}$ plates identified as the θ'-phase form chains along the dislocation lines [1,2,21]. They were found in the alloy at both ageing temperatures but are not shown here. For both peak-aging conditions, the precipitates with $\{111\}_{Al}$

habit planes were identified as the main strengthening agents. Comparing Figs. 1a and b, it was found that aging at 190 °C produces a more bimodal plate diameter distribution than at 150 °C, i.e. a combined fraction of coarse plates with a fraction of smaller plates with a narrow diameter (Figs. S1a and S1b in Supplementary Materials). The small plates at 190 °C have diameters comparable with the average one at 150 °C. The main difference between these two conditions is a three times higher precipitate number density at 150 °C compared to 190 °C.

Careful analysis of the $\{111\}_{Al}$ plates revealed that the majority of the plates had a thickness around 0.85 nm (comparable with 1 c_θ) as seen in Table 1. The most prominent feature is that the plates with this nominal thickness were found to be hybrid, comprising two inter-grown phase fragments. The plates with other thicknesses had non-hybrid structures.

Several structural features of the HPs can be identified in the $<110>_{Al}$ and $<211>_{Al}$ projections, as shown in Figs. 2a-d. Firstly, the projected Cu columns form a sub-lattice that demonstrates difference in shape/size of the inter-grown phase fragments (rectangular (θ) / rhombic (η) cells marked by yellow lines and circles in Figs. 2b and e). Secondly, there are distinct differences in atomic arrangement between the (here horizontal) layers of Cu-columns when comparing the two fragments. Thirdly, the amount of Cu in the layers near the middle (Cu_m) and at the interface (Cu_i) in the θ-fragments varies, as seen in Fig. 2b. Additionally, the concentration of Cu in Cu_m and Cu_i layers in the HPs are more similar than in the non-hybrid $\{111\}_{Al}$ plates, as shown for precipitates of three thicknesses in Fig. 2e. A ~10% difference reduction in cell/layer thickness of η as compared to θ was estimated in the same HPs (Figs. 2b and d). Finally, integrated image intensity profiles of the HP $\{111\}_{Al}$ planes, indicate that that heavy elements like Cu and Ag can occupy additional sites in the Cu_m layers (Figs. 2b and d), as compared to the non-hybrid $\{111\}_{Al}$ plates (Fig. 2e and S2b). The intensity profiles of the $\{211\}_{Al}$ projections for the non-hybrid plates suggest there are fewer or no extra atoms in interstitial sites of the Cu_m layers (Fig. 3e), as compared to the Cu_m layers [22] within the HP's (Figs. 2b and d).

The rectangular phase fragment in Fig. 2b is an orthorhombic building block for the non-HPs (Fig. 2e). It has dimensions a_θ = 4.96 Å, b_θ = 8.56 Å, c_θ = 8.48 Å, space group *Fmmm* [23], and has been suggested to represent the cell of the bulk Ω-phase [4,6,23–25]. The unit is the generally accepted structure of the Ω precipitate [3,22,25,26]. It is closely connected to the equilibrium θ-Al_2Cu phase (*I4/mcm*) in the Al-Cu alloys [26].

Except for the θ-type fragment, a literature survey of precipitate phases in other Al-based alloys showed that the structure of the unknown fragment with rhombic appearance (Fig. 2b) is similar to the hexagonal η-type phase ($P6_3/mmc$, $MgZn_2$). The possible formation of a hexagonal phase in Al-Cu-Mg-Ag alloys has already been predicted [23].

The following presumptions were used to construct the structural models of the HPs embedded in the Al matrix, in order to investigate the energetics (Fig. 3):

a) The Ag_2Mg and Cu_i layers [22], appearing as hexagonal arrangements in $\{111\}_{Al}$ projections (Fig. 3a), were used to model the η/Al and θ/Al interfaces.

b) Similar Cu arrangements were assumed for the Cu_i and Cu_m layers [22]. For the hybrid $\{111\}_{Al}$ plates the Cu_m layer was interpreted as enriched by Cu (Fig. 2b) in line with the Cu_m layers in the orthorhombic θ-phase (Fig. 2e) [22].

c) The atomic structure of the equilibrium η-phase in aged Al-Zn-Mg alloys [27–30] was used as template for the η-type fragment of the HP (Fig. 3), where Zn and Mg are substituted by Cu and Al atoms, respectively [27–30].

Two categories of plates were constructed to compare the energies of atomic configurations for the HP. The first category concerns the non-HP, fully comprised of θ-type fragments before relaxation (cf. mod. 1, Tables 2 and S4). For the second category, the HP's initially included the η- and θ-type phase fragments before relaxation (models 2-12, Tables 2 and S4). However, some models using only Al and Cu in the θ- and η-type fragments, which initially were suggested as HP structures, were found to transform structurally to non-HP, which signifies instability. For this

reason, the HP stabilization was checked also by substituting Al in the bulk structure. Another reason that substitution should be tested, is that traces of Mg, Ag and Cu have previously been reported in plate-shaped precipitates habiting $\{111\}_{Al}$ planes in Al-Cu-Mg-Ag alloys during the early aging stages [7].

From Table 2 can be seen that refinement of atom positions (*p*) of the models gives favorable energies, and that full relaxation of geometry (*f*) gives a further improvement. The relaxations caused fundamentally different atom displacements in the non-HP model (comprised of θ-type fragments before relaxation - model 1 from Tables 2 and S4, Fig. S2) compared to the HP model (with the η- and θ-type phase fragments - model 2 from Tables 2 and S4, Fig. S3). For model 1 the atom displacements led to minor column distortions relative to the Al matrix and the orthorhombic θ-phase (Figs. S2). For the model 2 it led to transformation to non-HP structures based on model 1 (Fig. S3).

DFT calculations (Fig. 4, Tables 2 and S4) show that the non-HP obtained after *p* and *f* relaxation of model 2 (starting with the HP configuration) has lower formation enthalpy compared to the non-HP model 1 (Fig. 4, Table 2). The lower enthalpy correlates with a larger cooperative atom displacement in the $\{111\}_{Al}$ planes in the non-HP model 1 (~0.12-0.15 nm, in Fig. S2) compared to the HP model 2 (~0.05 nm, Fig. S3c). It is obvious that atom orderings in the Ag_2Mg interface layers of the plates with the thickness about one θ unit cell should be similar to each other and correspond to the *A* stacking of the fcc matrix as shown in Figs. S2b and S3, in order to reduce the precipitate formation enthalpy (E_f). E_f includes a shear strain field energy (E_S) caused by the structural incompatibility at the broad precipitate/Al interfaces [8,9] and the volumetric strain energy due to the precipitate volume inconsistency with the Al matrix in the $[111]_{Al}$ directions (ε_c) [3] and with the $\{111\}_{Al}$ planes (ε_p given in Tables 2 and S4). Consequently, several strain accommodation mechanisms as well as their superposition are important for reducing E_f. It should be noted that the shear itself should not change the misfit strain in $[111]_{Al}$, but this unrelaxed misfit can promote a change in W_S , which is inversely proportional to the interplane spacing ($W_S \sim 1/d_{111}$)

[31]. Thus, the thicker plates have larger unrelaxed misfits which help to effectively reduce E_S and suppress the formation of the η-type fragment. The plates with thickness of 0.5 c_θ does not have the η-type structure because of the precipitate chemistry. Its bulk and interface structures are slightly different. The reason is solute segregations from the orthorhombic θ lattice and the Ag_2Mg and Cu_i layer arrangements suggested in [22] which is also used in our calculations.

Using direct measurements of the distances between the Cu_i layers in experimental ADF-STEM images, ε_c was calculated to be 4.5±1.0% for the non-HP and 4.2±1.2% for the HP. It is seen that ε_c for the non-HP is significantly lower than the 9.3% misfit evaluated on the basis of lattice parameters alone [25,32,33]. This inconsistency may support the observations that solutes with larger atomic size like Mg enter the precipitate structure in order to reduce misfit strain [7]. It is seen from our DFT calculations that for the non-HPs containing Mg, E_f values are lower for all the models including the non-HPs with Al and Cu (model 9 after *p* and *f* relaxations in Fig. 4, Table S4).

The ε_c values measured after DFT calculations were also estimated to be in the range from 4.8% to 8.9% for the most energetically favorable non-HP model 9 (with Mg) and the non-HP model 2 after *f* relaxation, respectively, and 7 % for the HP model 10. It seems that this large difference in ε_c from the values measured in ADF-STEM images may also be caused by solute segregations within the bulk and at the interfaces (2). In the latter case, note the substitution of Ag at the broad plate interfaces as marked in Figs. 2b and d.

Among all the HP configurations checked in the present study, model 10 refined to the lowest E_f, within the range of E_f values for the non-HPs containing Al and Cu. This model was used to simulate the STEM images. It can be seen that the simulated atom column distributions and intensities compare well with the experimental images, i.e. in Figs. 3b and c, respectively, which lends strong support to model 10.

It is interesting that for all models of HP and non-HPs (for both *p* and *f* relaxations), the Mg and Ag atoms in the Ag_2Mg layers, as well as the Cu atoms in the Cu_i layers at the main interfaces

keep an energetically favorable hexagonal symmetry in the $\{111\}_{Al}$ projection. This was previously shown in [22]. Note also that the main $\{111\}_{Al}$ plate/Al interface configuration is isostructural to that of η' precipitates in Al-Zn-Mg alloys [30] and the T1 phase in Al-Cu-Li alloys [34]. In fact, the HP structure with interface, as shown in Fig. 2b and the model (Fig. 3a) are isostructural with type 1 η' plate found in Al-Mg-Zn alloys [30]. The η-type fragment as marked here is structurally related to the Mg_4Zn_7 monoclinic phase in Mg-Zn(-Y) alloys [35].

In conclusion, this study has shown that a unique type of hybrid precipitate acts as the main strengthening agent in peak-aged Al-Cu-Mg-Ag. Formation of these precipitates is interpreted as a consequence of a structural incompatibility between the Al matrix and the pure θ-phase structure. Using DFT calculations, an energetically favorable structure with low specific volumetric strain energy was found, where incorporations of Cu, Mg and Ag were found necessary to stabilize the structure. A good match between the experimental and simulated STEM images supports the model.

The authors are grateful to the staff at the TEM Gemini Center at NTNU, the Joint Research Center at Belgorod State University and Skolkovo Institute of Science and Technology for their assistance with the structural analysis, mechanical characterizations, and computations, respectively.

Funding: The TEM work was supported by the Faculty of Natural Sciences at the Norwegian University of Science and Technology (NTNU), Trondheim, Norway [grant number 81617879] using the NORTEM infrastructure (grant number NFR197405) at the TEM Gemini Centre. Mechanical tests were financed by the Ministry of Science and Higher Education of the Russian Federation, Russia [grant number 14.584.21.0023]. STEM image simulations were supported by Act No. 211 from 16 March 2013 of the Government of the Russian Federation (contract number 02.A03.21.0011).

References

[1] I.J. Polmear, Light Alloys: From Traditional Alloys to Nanocrystals, third ed., Butterworth-Heinemann/Elsevier, Oxford (UK), 2006.

[2] J.F. Nie, Physical Metallurgy of Light Alloys, Fifth Edit, Elsevier, 2014.

[3] C.R. Hutchinson, X. Fan, S.. Pennycook, G.. Shiflet, Acta Mater. 49 (2001) 2827–2841.

[4] S. Abis, P. Mengucci, G. Riontino, Philos. Mag. B Phys. Condens. Matter; Stat. Mech. Electron. Opt. Magn. Prop. 67 (1993) 465–484.

[5] J.A. Taylor, B.A. Parker, I.J. Polmear, Met. Sci. 12 (1978) 478–482.

[6] S. Kerry, V.D. Scott, Met. Sci. 18 (1984) 289–294.

[7] L. Reich, M. Murayama, K. Hono, Acta Mater. 46 (1998) 6053–6062.

[8] H.I. Aaronson, B.C. Muddle, J.F. Nie, Scr. Mater. 41 (1999) 203–208.

[9] J.F. Nie, H.. Aaronson, B.C. Muddle, in: M. Tiyakioglu, M. Tiyakioglu (Eds.), Adv. Metall. Alum. Alloy., Indianapolis, 2001, pp. 229–238.

[10] M. Gazizov, R. Holmestad, R. Kaibyshev, IOP Conf. Ser. Mater. Sci. Eng. 672 (2019).

[11] M. Gazizov, C.D. Marioara, J. Friis, S. Wenner, R. Holmestad, R. Kaibyshev, J. Alloys Compd. 826 (2020) 153977.

[12] L. Jones, H. Yang, T.J. Pennycook, M.S.J. Marshall, S. Van Aert, N.D. Browning, M.R. Castell, P.D. Nellist, Adv. Struct. Chem. Imaging 1 (2015) 1–16.

[13] W. Kohn, L.J. Sham, Phys. Rev. 240 (1985) A1133.

[14] E. Blochl, Phys. Rev. B 50 (1994) 17953–17979.

[15] J.P. Perdew, K. Burke, M. Ernzerhof, Phys. Rev. Lett. 77 (1996) 3865–3868.

[16] G. Kresse, J. Furthmüller, Comput. Mater. Sci. 6 (1996) 15–50.

[17] D.A. Aksyonov, S.S. Fedotov, K.J. Stevenson, A. Zhugayevych, Comput. Mater. Sci. 154 (2018) 449–458.

[18] I. Lobato, S. Van Aert, J. Verbeeck, Ultramicroscopy 168 (2016) 17–27.

[19] I. Lobato, D. Van Dyck, Ultramicroscopy 156 (2015) 9–17.

[20] I. Lobato, D. Van Dyck, Acta Crystallogr. Sect. A 70 (2014) 636–649.

[21] M. Gazizov, R. Kaibyshev, Mater. Sci. Eng. A 702 (2017) 29–40.

[22] S.J. Kang, Y.W. Kim, M. Kim, J.M. Zuo, Acta Mater. 81 (2014) 501–511.

[23] K.M. Knowles, W.M. Stobbs, Acta Crystallogr. Sect. B Struct. Sci. 44 (1988) 207–227.

[24] J.H. Auld, Mater. Sci. Technol. 2 (1986) 784–787.

[25] B.C. Muddle, I.J. Polmear, Acta Metall. 37 (1989) 777–789.

[26] S.C. Wang, M.J. Starink, Int. Mater. Rev. 50 (2005) 193–215.

[27] M. Dumont, W. Lefebvre, B. Doisneau-Cottignies, A. Deschamps, Acta Mater. 53 (2005) 2881–2892.

[28] S.S. Brenner, J. Kowalik, Hua Ming-Jian, Surf. Sci. 246 (1991) 210–217.

[29] A. Deschamps, A. Bigot, F. Livet, P. Auger, Y. Bréchet, Philos. Mag. A Phys. Condens. Matter, Struct. Defects Mech. Prop. 81 (2001) 2391–2414.

[30] C.D. Marioara, W. Lefebvre, S.J. Andersen, J. Friis, J. Mater. Sci. 48 (2013) 3638–3651.

[31] R.W.K. Honeycombe, The Plastic Deformation of Metals, 2nd ed., Hodder Arnold, New York, 1984.

[32] A. Garg, J.M. Howe, Acta Metall. Mater. 39 (1991) 1939–1946.

[33] S.P. Ringer, K. Hono, I.J. Polmear, T. Sakurai, 44 (1996) 1883–1898.

[34] C. Dwyer, M. Weyland, L.Y. Chang, B.C. Muddle, Appl. Phys. Lett. 98 (2011) 201909.

[35] J.M. Rosalie, H. Somekawa, A. Singh, T. Mukai, Philos. Mag. 91 (2011) 2634–2644.

FIGURE CAPTIONS

Figure 1. STEM images representing a typical precipitate microstructure in the alloy peak-aged at 150 °C (a) and 190 °C (b).

Figure 2. STEM images showing the hybrid (a-d) and non-hybrid $\{111\}_{Al}$ plates (e). Fast Fourier transform (FFT) filtering was applied (in b, d, and e) to reduce noise with a periodicity shorter than ~0.05 nm. For each image, fast and slow scanning directions are marked as 'fs' and 'ss', respectively. Non-uniform oscillation of the atomic column intensity along the interface, as indicated by orange arrows, can be evidence of the difference in chemistry between the atom columns.

Figure 3. The models including the HP (a); simulated (b) and experimental denoised STEM images (c). The projection scale was reduced by a factor of 0.5 in $[2\text{-}1\text{-}1]_{Al}$. 12 variants of the HP with substitution of the Al atoms in sites #1 – #4 by Cu, Mg and Ag have been checked to find the energetically favorable one (Tables 2 and S4). In STEM image simulations, the elastic electron scattering factors were parameterized as in [20]. The same Debye-Waller factor of 0.5 $Å^{-2}$ was chosen for Al, Cu, Mg and Ag. The sample thicknesses were the same as respective sizes of the DFT model (~10 Å for $\{110\}_{Al}$ and $\{211\}_{Al}$ projections). The electron probe parameters (spot size, convergence and collection semi-angles, etc.) were set in the MULTEM software as in our TEM experiments.

Figure 4. Formation enthalpies for the suggested models. Cyan and red rectangles, and dashed lines and dotted lines in these rectangles refer to the models including the non-HP and HP, and to the formation enthalpies after *f*/*p* relaxations and their average, respectively.

Figure 1

Click here to access/download;Figure(s);Fig 2.tif

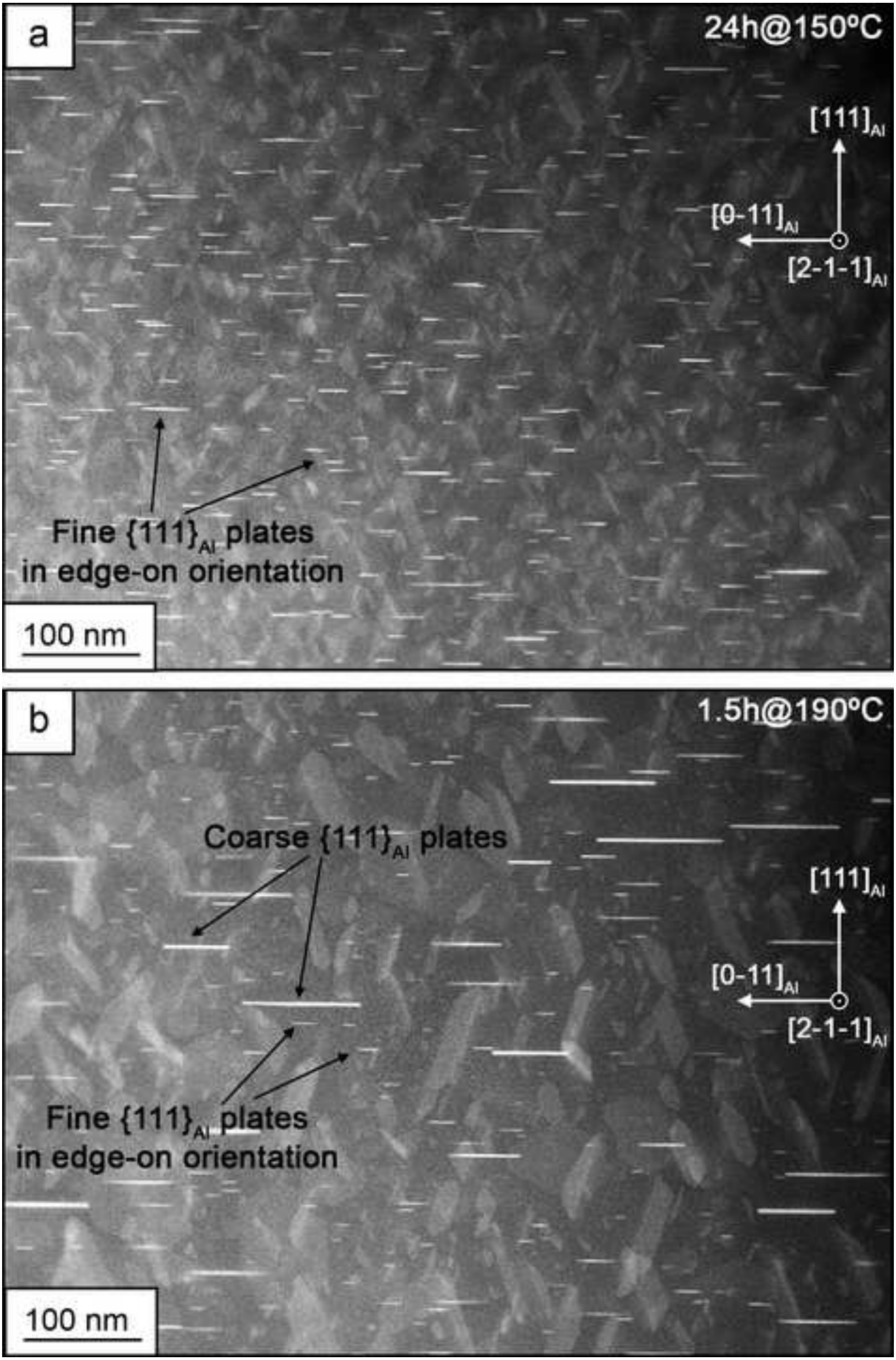

Figure 2

Click here to access/download;Figure(s);Fig 3.tif

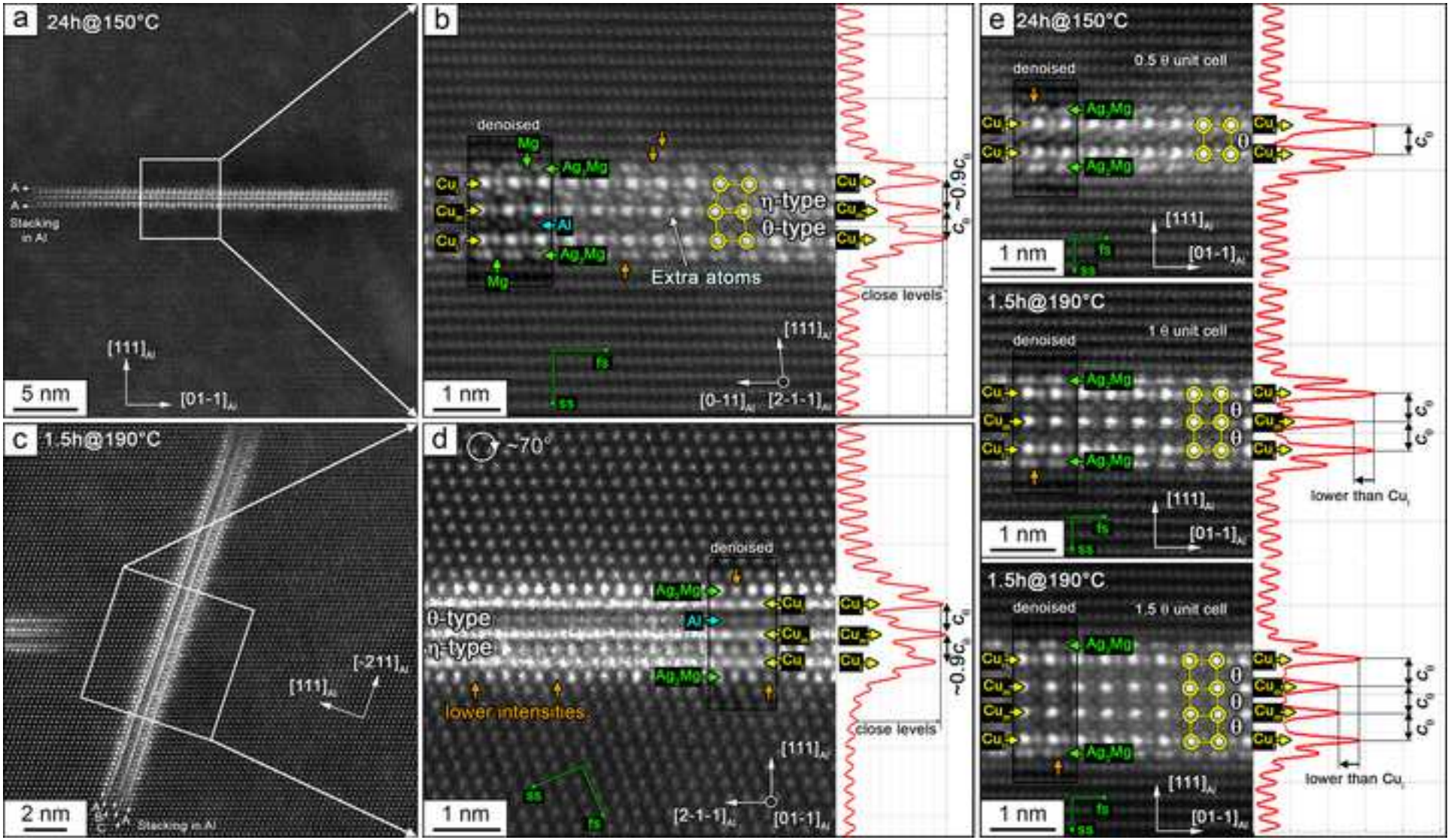

Figure 3

Click here to access/download;Figure(s);Fig 4.tif

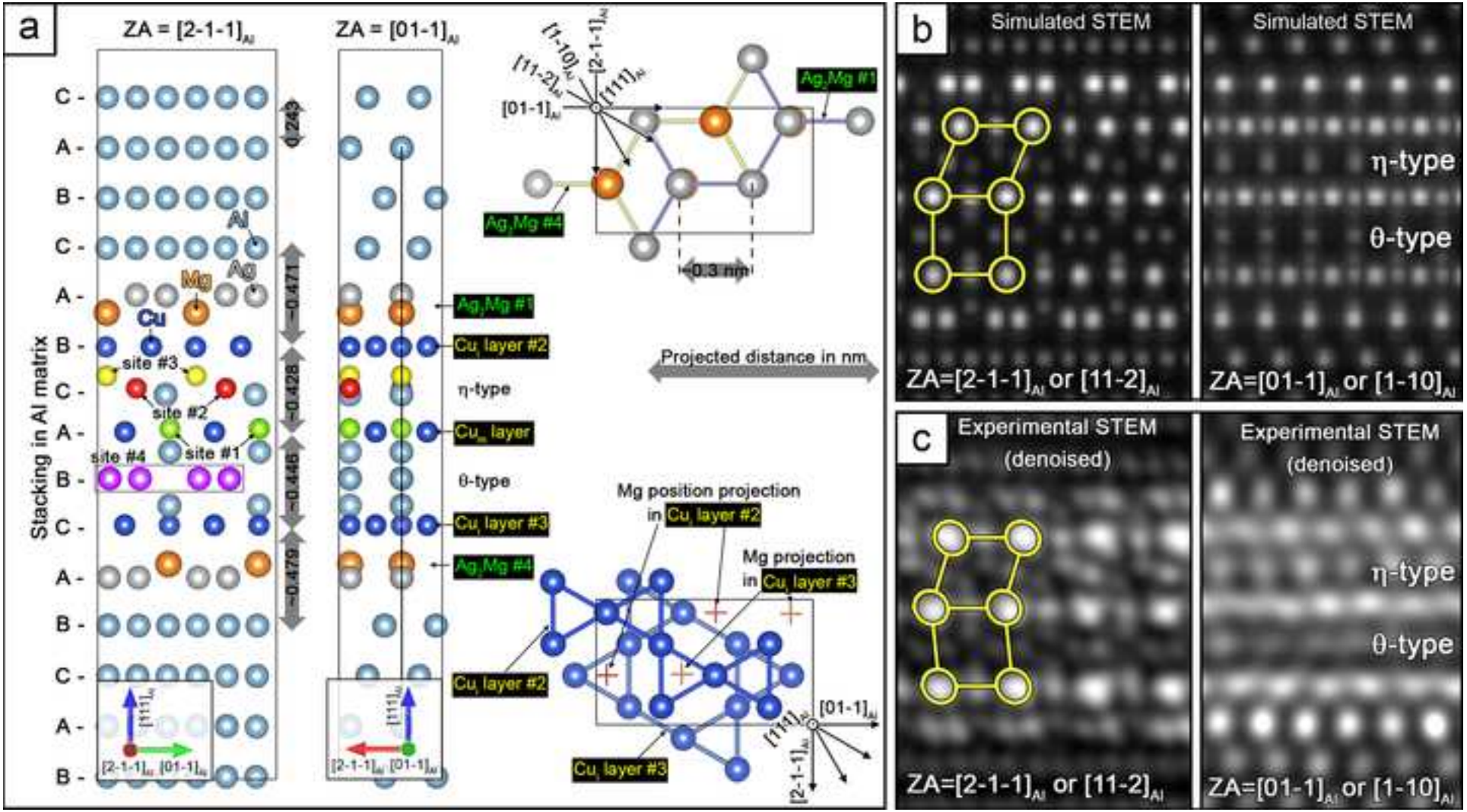

Figure 4

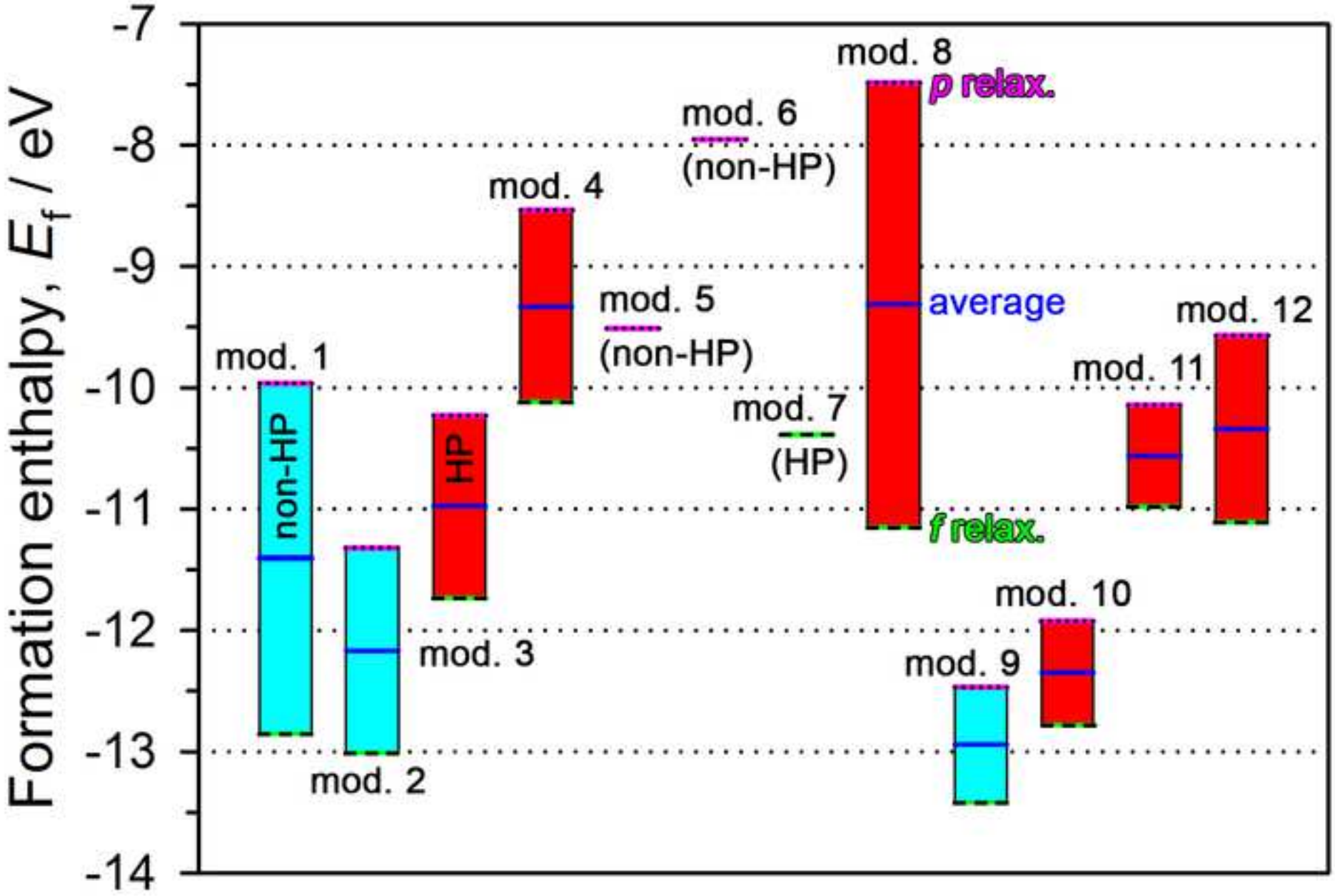

TABLES

Table 1. The $\{111\}_{Al}$ plates with different thicknesses analyzed by TEM.

Aging state	Plate thickness, in terms of θ unit cells (c_θ =0.848 nm)							
	0.5	1	1.5	2	2.5	3	3.5	4
150°C for 24 h	12	33 (33*)	-	1	2	0	1	-
190°C for 1.5 h	15	40 (35*)	3	5	4	-	-	-

* - total number of HPs identified in each state.

Table 2. Formation enthalpies (E_f) for the models, including the non-hybrid (mod. 1) and hybrid $\{111\}_{Al}$ precipitate models. After atom position (*p*) and full (*f*) relaxations, the HP models tended to transform to the non-HPs. Direct (D) transformation from the η- to θ-type fragments (η→θ) are marked. The full table is given in Supplementary Materials (Table S4). The precipitate misfit in $[111]_{Al}$ was calculated as $\varepsilon_c = (t - Nd_{111})/Nd_{111}$, where t is the distance between the Cu_i layers in the models, d_{111} is the spacing between the $\{111\}_{Al}$ layers measured in the bulk Al matrix; N is the number of the $\{111\}_{Al}$ layers, thickness of which closely matches the thickness of the phase fragments. The volume incompatibility between the Al matrix and precipitate in $\{111\}_{Al}$ was calculated as $\varepsilon_c = (S_f - S_{Al})/S_{Al}$, where S_f and S_{Al} are the cross-section areas for the models after *f* relaxation and the reference $\{111\}_{Al}$ plane, respectively.

Model *n*	Relaxation	E_f, eV	Sites in the HP				Transformation	ε_c in $[111]_{Al}$, %	ε_p in $\{111\}_{Al}$, %
			#1	#2	#3	#4			
Non-hybrid $\{111\}_{Al}$ plates entirely comprising of the θ-type fragments before relaxation									
1	p	-9.96	-	-	-	-	-	-7.8	1.4
	f	-12.85	-	-	-	-	-	-7.9	
Hybrid $\{111\}_{Al}$ plates comprising of the θ- and η-type fragments before relaxation									
2	p	-11.32	Al	Al	Al	Al	D	-8.9	1.5
	f	-13.01	Al	Al	Al	Al	D	-8.9	
9	p	-12.46	Al	Al	Al	Mg	D	-5.3	1.3
	f	-13.42	Al	Al	Al	Mg	D	-4.8	
10	p	-11.92	Cu	Al	Al	Mg	-	-8.0	0.9
	f	-12.78	Cu	Al	Al	Mg	-	-7.0	